

ARTICLE

Open Access

# Formamidinium lead triiodide perovskites with improved structural stabilities and photovoltaic properties obtained by ultratrace dimethylamine substitution

Wen-Cheng Qiao<sup>1</sup>, Jia-Qi Liang<sup>1</sup>, Wei Dong<sup>1</sup>, Kaiyang Ma<sup>1</sup>, Xue Lu Wang<sup>1</sup>  and Ye-Feng Yao<sup>1</sup> 

## Abstract

Applications of organic–inorganic formamidinium (FA) lead triiodide (FAPbI<sub>3</sub>) perovskites in high-efficiency solar cells often suffer from spontaneous  $\alpha$ -to- $\delta$  phase transitions. However, current efforts to inhibit this phenomenon based on simple cation and anion alloying strategies continue to suffer from unintended consequences, such as unfavorable shifts in the bandgap energy and unwanted phase separation during operation. The present work compares the effects of bromine (Br) anion and dimethylamine (DMA) cation alloying on the structure and properties of FAPbI<sub>3</sub> perovskite in detail. DMA-incorporated FAPbI<sub>3</sub> perovskites show significantly improved structural stability and photovoltaic performance, while the inherent bandgap energy of the original material is maintained. Rigorous analyses demonstrate that the relatively large size and free isotropic motion of the incorporated DMA cations constrain the dynamic space of neighboring FA cations, which increases the degree to which the FA cations interact with the inorganic lattice and therefore stabilizes the PbI<sub>6</sub> lattice structure without significant lattice distortion. Hence, this work demonstrates an efficient method for improving the phase stability of FAPbI<sub>3</sub> perovskite materials while providing a plausible molecular mechanism for the stability engendered by the alloying of DMA and FA.

## Introduction

Organic–inorganic halide perovskite semiconductor materials have been widely used in a variety of photovoltaic devices, such as perovskite solar cells (PSCs)<sup>1–3</sup>, light-emitting diodes<sup>4–6</sup>, and photodetectors<sup>7–9</sup>, owing to their excellent photovoltaic properties<sup>10,11</sup> and easy, low-cost preparation<sup>12</sup>. In fact, well-designed perovskite PSCs have achieved power conversion efficiency (PCE) values as high as 25.2%<sup>13</sup>, which is comparable to those of conventional silicon-based solar cells<sup>14</sup>. Most PSC materials employ organic formamidinium (FA) or methylamine (MA) cations in conjunction with inorganic PbI<sub>3</sub>

perovskite components<sup>15</sup>. Among these, FAPbI<sub>3</sub> is generally preferred to MAPbI<sub>3</sub> owing to its better thermal stability<sup>16</sup>, better charge carrier transport properties<sup>17</sup>, and narrower bandgap energy extending into the near infrared (NIR) region<sup>18,19</sup>. However, practical PSC applications based on FAPbI<sub>3</sub> are seriously limited by the spontaneous transformation of the photovoltaically active black  $\alpha$ -phase of FAPbI<sub>3</sub> to the unwanted but more stable yellow  $\delta$ -phase of FAPbI<sub>3</sub> at room temperature<sup>20</sup>.

This issue is effectively addressed via various cation alloying and/or anion alloying strategies, which have demonstrated dramatic improvements in both the stability and photoelectric efficiency of FAPbI<sub>3</sub> materials<sup>21–23</sup>. For example, past studies have demonstrated that substituting FA cations with much smaller inorganic cations, such as Cs<sup>24</sup> and Rb<sup>25</sup>, can enhance the stability of FAPbI<sub>3</sub> by adjusting the Goldschmidt tolerance factor associated

Correspondence: Xue Lu Wang (xlwang@phy.ecnu.edu.cn) or Ye-Feng Yao (yfiao@phy.ecnu.edu.cn)

<sup>1</sup>Physics Department & Shanghai Key Laboratory of Magnetic Resonance, School of Physics and Electronic Science, East China Normal University, North Zhongshan Road 3663, Shanghai 200062, People's Republic of China

© The Author(s) 2022



**Open Access** This article is licensed under a Creative Commons Attribution 4.0 International License, which permits use, sharing, adaptation, distribution and reproduction in any medium or format, as long as you give appropriate credit to the original author(s) and the source, provide a link to the Creative Commons license, and indicate if changes were made. The images or other third party material in this article are included in the article's Creative Commons license, unless indicated otherwise in a credit line to the material. If material is not included in the article's Creative Commons license and your intended use is not permitted by statutory regulation or exceeds the permitted use, you will need to obtain permission directly from the copyright holder. To view a copy of this license, visit <http://creativecommons.org/licenses/by/4.0/>.

with the stability of the  $\alpha$ - and  $\delta$ -phases. Similarly, the partial incorporation of MA cations into FAPbI<sub>3</sub> has been demonstrated to stabilize the  $\alpha$ -phase by facilitating stronger hydrogen bonds with the inorganic lattice<sup>26,27</sup>. Other studies have demonstrated that the partial incorporation of Br anions in FAPbI<sub>3</sub> can also stabilize the  $\alpha$ -phase<sup>28,29</sup>. Moreover, a synergistic effect on  $\alpha$ -FAPbI<sub>3</sub> stability has been demonstrated by a combined cation and anion alloying strategy, resulting in a new highly stable (FAPbI<sub>3</sub>)<sub>0.9</sub>(MAPbBr<sub>3</sub>)<sub>0.05</sub>(CsPbBr<sub>3</sub>)<sub>0.05</sub> mixed cation and mixed halide perovskite composition<sup>30,31</sup>. However, while considerable success has been obtained by these various alloying strategies, the increased stability and photoelectric efficiency have often been accompanied by unintended consequences<sup>32</sup>. For instance, the incorporation of Br may induce a blueshift of the bandgap, deviating from the ideal Shockley–Queisser limit<sup>33</sup>, and concurrently introduce a risk of phase segregation under illumination<sup>34,35</sup>. However, MA-containing perovskites may suffer from poor long-term stability in devices due to the low thermal stability of MA molecules<sup>36</sup>. The negative consequences significantly restrict the large-scale development of FAPbI<sub>3</sub>-based PSC applications. Addressing these issues has generated considerable interest in the field of perovskite alloying for PSC applications.

The present work addresses these issues by incorporating an ultratrace dimethylamine (DMA) for FAPbI<sub>3</sub>-based PSC applications. Here, the DMA cation [(CH<sub>3</sub>)<sub>2</sub>NH<sub>2</sub><sup>+</sup>] has an ionic radius of 272 pm, which is slightly greater than that of the FA cation (253 pm), and a greater number of hydrogen atoms than FA and therefore favors greater interactions with the inorganic perovskite lattice<sup>37</sup>. These factors enable DMA to be used in very small concentrations as an alternative cation for stabilizing  $\alpha$ -FAPbI<sub>3</sub> and thereby avoiding unintended effects. In addition, it is usually believed that the choice of A-site cations in 3D perovskite cages is limited by the empirical Goldschmidt tolerance factor, and 3D perovskites tend to form when  $0.8 < t < 1.0$ <sup>38</sup>. According to this theory, DMA seems to be too large to be incorporated into the lead iodine 3D lattice. However, many recent reports indicate that this tolerance factor theory might not be suitable for perovskites containing more complex organic cations<sup>39</sup>. For example, although hydroxylammonium and hydrazinium cations have nearly the same size as MA<sup>40</sup>, these cations cannot be incorporated into the PbI<sub>3</sub> framework. Furthermore, it was reported that the large cation DMA can be easily incorporated into 3D perovskites by a cation alloying strategy<sup>41</sup>.

In this work, the phase stability, bandgap energy, charge carrier behavior, and molecular dynamics of mixed-cation FA<sub>1-x</sub>DMA<sub>x</sub>PbI<sub>3</sub> perovskite ( $x = 0, 0.016, 0.025$ ) single-crystal samples are subjected to a wide range of analyses, including the measurement of visible-NIR (Vis-NIR)

absorption spectra, steady-state and time resolved (TR) photoluminescence (PL) measurements, photoresponse measurements of planar-type photodetector devices, differential thermal analysis (DTA), X-ray diffraction (XRD) measurements, and static <sup>1</sup>H, <sup>207</sup>Pb, and <sup>2</sup>H nuclear magnetic resonance (NMR) spectroscopy measurements. The details of the fabrication processes and characterization methods are presented in the Supporting Information (SI). We also compare these extensive analyses with those obtained for mixed-halogen FAPb(I<sub>1-y</sub>Br<sub>y</sub>)<sub>3</sub> ( $y = 0.05, 0.1$ ) perovskite. These rigorous analyses demonstrate that the proposed DMA substitution strategy can significantly improve the phase stability against water-oxygen infiltration and thermal cycling, and the photoelectric response is enhanced, while the inherent bandgap energy is maintained. Moreover, these analyses demonstrate that the molecular dynamic mechanism leading to the high structural stability obtained by DMA incorporation is quite different from that of the Br-incorporated samples. Here, the relatively large size and free isotropic motion of the incorporated DMA cations constrain the dynamic space of FA cations, which greatly increases the degree to which FA cations interact with the inorganic lattice and therefore stabilizes the PbI<sub>6</sub> lattice structure without significant lattice distortion. In contrast, the structural stability obtained by Br substitution is attributable to the significant degree of lattice distortion arising from the mismatch between the different Pb environments produced under Br substitution, which stabilizes the phase of the lattice structure but also results in lower crystallinity and an unwanted change in the bandgap energy. Accordingly, this work demonstrates an efficient method for improving the phase stability of organic–inorganic FAPbI<sub>3</sub> perovskite semiconductor materials and provides plausible molecular mechanisms for the stability engendered by cation and halogen alloying in FA-based perovskites.

## Materials and methods

### Materials synthesis

Deuterated ND<sub>2</sub>CH = ND<sub>2</sub>I (FA(d4)I) was synthesized by dissolving FAI in deuterium oxide with a 1:20 molar ratio in a 50 mL flask, followed by vacuum freeze-drying to remove the solvent. This process was repeated three times to obtain the final deuterated precursor.

### Growth of FA<sub>1-x</sub>DMA<sub>x</sub>PbI<sub>3</sub> single crystals

A solution containing FAI, DMAI, and PbI<sub>2</sub> in a molar ratio of (1 - x): x: 1 ( $x = 0, 0.05, 0.07$ ) was prepared in  $\gamma$ -butyrolactone (GBL) at room temperature (20 °C). The solutions were filtered using a polytetrafluoroethylene (PTFE) filter with a 0.2 mm pore size, heated to 110 °C, and held at that temperature until the desired single crystals formed. The maximum value of  $x$  was selected

based on the fact that the DMA-incorporated  $\text{FAPbI}_3$  single crystals are unable to grow from the precursor solution when  $x > 0.07$ . The DMA-containing  $\text{FAPbI}_3$  single crystals are tentatively named  $\text{FA}_{0.95}\text{DMA}_{0.05}$  and  $\text{FA}_{0.93}\text{DMA}_{0.07}$  based on the stoichiometry of the substrates used in the synthesis. A similar procedure was employed to synthesize the corresponding deuterated N-deuterated  $\text{FA}(\text{d4})_{1-x}\text{DMA}_x\text{PbI}_3$  and C-deuterated  $\text{FA}_{1-x}\text{DMA}(\text{d6})_x\text{PbI}_3$  single crystals. The shapes and sizes of the obtained single crystals were consistent at all values of  $x$  considered (Fig. S1).

### Growth of $\text{FAPbPb}(\text{I}_{1-y}\text{Br}_y)_3$ single crystals

For Solution 1, an equimolar mixture of  $\text{FAI}$  and  $\text{PbI}_2$  was dissolved in GBL, and the solution concentration was controlled at 1.2 M. For Solution 2, an equimolar mixture of  $\text{FABr}$  and  $\text{PbBr}_2$  was dissolved in DMF, and the solution concentration was controlled at 1.2 M. Specific volumes of Solution 1 and Solution 2 were mixed in glass vials according to the desired value of  $y$ . Finally, the mixed precursor solutions were filtered using a PTFE filter with a 0.2  $\mu\text{m}$  pore size, heated to 110  $^\circ\text{C}$ , and held at that temperature until the desired  $\text{FAPb}(\text{I}_{1-y}\text{Br}_y)_3$  ( $y = 0.05, 0.1$ ) single crystals formed. A similar procedure was employed to synthesize the corresponding deuterated  $\text{FA}(\text{d4})\text{Pb}(\text{I}_{1-y}\text{Br}_y)_3$  single crystals.

### Fabrication and photoresponse measurements of photodetector devices

Planar-type photodetector devices (Fig. S2) were fabricated by depositing Au electrodes via vacuum evaporation on the top surface of the single-crystal samples. The Au electrodes were 0.76 mm in length and 60  $\mu\text{m}$  in width, with a thickness of approximately 100 nm, while the bridging-gap width of the electrodes was 80  $\mu\text{m}$ . The effective absorber area of each device was 0.0608  $\text{mm}^2$ . The photoresponse characteristics of the photodetectors were collected under varying bias voltages using a Keithley 2400 source meter under pulsed illumination conditions at 1 Hz from a solar simulator with an optical power density of 20  $\text{mW}/\text{cm}^2$ .

### Powder X-ray diffraction (XRD)

Single-crystal samples were ground into fine powder, and powder XRD was conducted at room temperature using a Bruker AXS D8 diffractometer operated at 40 kV and 30 mA with  $\text{CuK}\alpha$  radiation ( $\lambda = 1.54186 \text{ \AA}$ ).

### Long-term water-oxygen stability testing

The fine powder samples were stored in an incubator at room temperature with a relative humidity of 65% for more than 150 days, and the samples were characterized at daily intervals by using powder XRD.

### Visible and near infrared (Vis-NIR) absorption spectra measurement

Vis-NIR absorption spectra were obtained at room temperature in the 600–900 nm region using a Lambda 950 spectrophotometer (PerkinElmer, USA) with an integrating sphere attachment.

### Steady-state and time resolved (TR) photoluminescence (PL) measurements

Standard static-state PL measurements were conducted at room temperature over the 650–950 nm range using a Renishaw in Via Reflex Raman microscope with a 625 nm laser as the excitation source. The TR-PL measurements were conducted at room temperature using a PicoQuant Fluor Time 300 fluorescence spectrometer with a 625 nm pulsed laser diode as the excitation source.

### Thermal analysis

Single-crystal samples were ground into fine powder, and thermogravimetric analysis (TGA) was conducted with a TA Instruments SDT-Q600 analyzer. During testing, approximately 5 mg of an-prepared single crystal powder was transferred into an  $\text{Al}_2\text{O}_3$  crucible and heated from room temperature to 600  $^\circ\text{C}$  at a ramp rate of 5  $^\circ\text{C}/\text{min}$  under flowing  $\text{N}_2$  gas.

### Nuclear magnetic resonance (NMR) spectroscopy

Single-crystal samples were ground into fine powder and immediately subjected to NMR spectroscopy measurements.  $^1\text{H}$  NMR spectra were acquired at room temperature using a Bruker Avance HD X500 500 MHz spectrometer. The individual samples were prepared by dissolving a small portion of the dried powder (~10 mg) in a  $\text{DMSO-d}_6$  solution (0.5 mL). The delay time was set to 30 s to allow for complete relaxation between experiments.  $^{207}\text{Pb}$  NMR spectra,  $^2\text{H}$  NMR spectra and  $^2\text{H}$  saturation recovery  $T_1$  measurements were acquired using a Bruker Avance III 300 MHz spectrometer equipped with a two-channel static polarization enhancement (PE) probe with a custom made 2.5 mm coil. The  $^{207}\text{Pb}$  spectra were acquired using a single-pulse excitation pulse sequence with a recycle delay of 2 s. All  $^{207}\text{Pb}$  NMR spectra were referenced to  $\text{PbMe}_4$  ( $\delta(^{207}\text{Pb}) = 0 \text{ ppm}$ ) by setting the measured  $^{207}\text{Pb}$  peak of  $\text{MAPbCl}_3$  to  $-647.5 \text{ ppm}$ . The  $^2\text{H}$  spectra were acquired using a solid echo pulse sequence. The  $^2\text{H}$  pulse width was 2  $\mu\text{s}$  at a radio frequency (RF) field strength of  $\gamma B_1/2\pi = 125 \text{ kHz}$  with a recycle delay of 2 s. The  $^2\text{H}$  patterns were simulated via the weblab (<http://weblab.mpip-mainz.mpg.de/weblab/>).

## Results and discussion

### Lattice structure of $\text{FA}_{1-x}\text{DMA}_x\text{PbPbI}_3$ and $\text{FAPb}(\text{I}_{1-y}\text{Br}_y)_3$

The quantitative  $^1\text{H}$  NMR spectra shown in Fig. S3 verifies that the actual molar ratios of  $\text{DMA}/(\text{DMA} + \text{FA})$

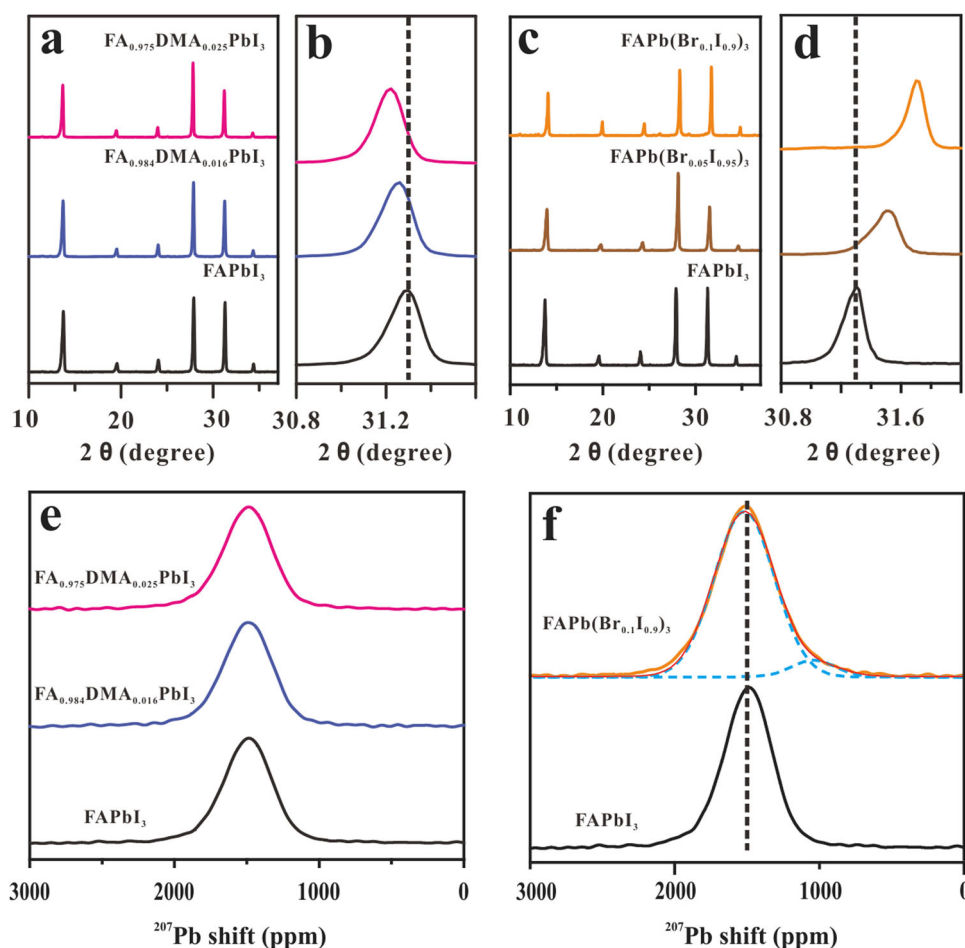


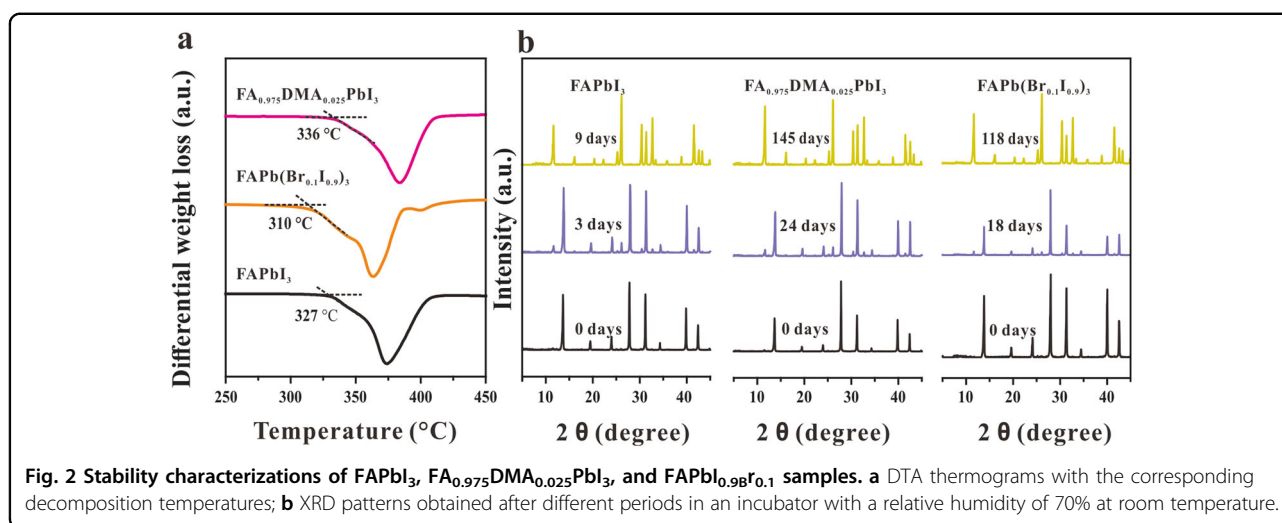
**Fig. 1** Lattice structure characterizations of  $\text{FAPbI}_3$ ,  $\text{FA}_{0.975}\text{DMA}_{0.025}\text{PbI}_3$ , and  $\text{FAPbI}_{0.9}\text{Br}_{0.1}$  samples. Powder XRD patterns of  $\text{FA}_{1-x}\text{DMA}_x\text{PbI}_3$  ( $x = 0, 0.016$ , and  $0.025$ ) perovskite samples: **a** overall patterns; **b** single diffraction peak patterns in (a). Powder XRD patterns of  $\text{FAPb}(\text{I}_{1-y}\text{Br}_y)_3$  ( $y = 0, 0.05, 0.1$ ) perovskite samples: **c** overall patterns; **d** single diffraction peak patterns in (c). **e** Static  $^{207}\text{Pb}$  NMR spectra of  $\text{FA}_{1-x}\text{DMA}_x\text{PbI}_3$  ( $x = 0, 0.016, 0.025$ ) perovskite samples. **f** Static  $^{207}\text{Pb}$  NMR spectra of  $\text{FAPb}(\text{I}_{1-y}\text{Br}_y)_3$  ( $y = 0, 0.1$ ) perovskite samples, where the peak of  $\text{FAPb}(\text{I}_{0.95}\text{Br}_{0.05})_3$  has been fitted based on the two Gaussian curves (dashed blue lines) with the combined peak given by the solid red line.

in  $\text{FA}_{0.95}\text{DMA}_{0.05}$  and  $\text{FA}_{0.93}\text{DMA}_{0.07}$  are approximately 1.6 and 2.5%, respectively, indicating that trace amounts of DMA cations can be incorporated into the lattice of  $\text{FAPbI}_3$ . In the following, the DMA-containing  $\text{FAPbI}_3$  single crystals are renamed as  $\text{FA}_{0.984}\text{DMA}_{0.016}\text{PbPbI}_3$  and  $\text{FA}_{0.975}\text{DMA}_{0.025}\text{PbPbI}_3$  based on the actual molar ratios of DMA/FA. The detailed crystalline structures of the as-prepared  $\text{FA}_{1-x}\text{DMA}_x\text{PbPbI}_3$  ( $x = 0, 0.016$ , and  $0.025$ ) perovskite samples at room temperature can be compared based on the powder XRD patterns presented in Fig. 1a, b. The XRD patterns in Fig. 1a are nearly identical, indicating that the pure and DMA-containing samples all conform to the cubic crystal structure of  $\alpha$ -phase  $\text{FAPbI}_3$ . However, the results in Fig. 1b demonstrate that the diffraction peaks increasingly shift to lower values of  $2\theta$  with increasing DMA content. This indicates that DMA substitution produces some lattice expansion, which can be

attributed to the larger ionic radius of DMA relative to that of FA. Similar to what was observed in Fig. 2a, the XRD patterns obtained for  $\text{FAPb}(\text{I}_{1-y}\text{Br}_y)_3$  ( $y = 0, 0.05$ , and  $0.1$ ) in Fig. 1c indicate that the Br-containing samples also conform to the cubic crystal structure of  $\alpha$ -phase  $\text{FAPbI}_3$ . However, the diffraction peaks shown in Fig. 1d increasingly shift to higher values of  $2\theta$  with increasing Br content. This indicates that Br substitution results in lattice contraction, which can be attributed to the smaller ionic radius of Br relative to that of I.

The static  $^{207}\text{Pb}$  NMR spectra obtained for  $\text{FA}_{1-x}\text{DMA}_x\text{PbI}_3$  ( $x = 0, 0.016, 0.025$ ) perovskite samples at room temperature ( $\sim 293$  K) are presented in Fig. 1e. We note that the  $^{207}\text{Pb}$  signal of  $\text{FAPbI}_3$  appears as a wide isotropic peak centered at approximately 1491 ppm. This observation is in good agreement with previously published results<sup>42</sup>. Moreover, the  $^{207}\text{Pb}$  NMR signals of the





DMA-containing samples are nearly identical to those obtained for FAPbI<sub>3</sub>, indicating that DMA substitution has no obvious effect on the local environment of the Pb atoms in the perovskite lattice. In contrast, the static <sup>207</sup>Pb NMR spectra obtained for the FAPb(I<sub>1-y</sub>Br<sub>y</sub>)<sub>3</sub> ( $y = 0, 0.1$ ) perovskite samples presented in Fig. 1f exhibit obvious differences, where the <sup>207</sup>Pb NMR signal of FAPb(I<sub>0.9</sub>Br<sub>0.1</sub>)<sub>3</sub> has an asymmetric lineshape with an obviously increased peak width. Fitting the signal peak using two Gaussian curves yields two signal components centered at 1500 ppm and 956 ppm. Previous studies have assigned the peaks at 1500 ppm and 956 ppm to [PbI<sub>6</sub>]<sup>2-</sup> and [PbBr<sub>3</sub>I<sub>3</sub>]<sup>2-</sup>, respectively<sup>42,43</sup>. This result strongly indicates that the incorporation of Br produces a mixed Pb coordination environment. In addition, the large width of the [PbI<sub>6</sub>]<sup>2-</sup> signal component in FAPb(I<sub>0.9</sub>Br<sub>0.1</sub>)<sub>3</sub> likely results from local disorder in the Pb octahedra arising from the mismatch between the distinct Pb environments.

#### Structural stabilities and photovoltaic properties of FA<sub>1-x</sub>DMA<sub>x</sub>PbPbI<sub>3</sub> and FAPb(I<sub>1-y</sub>Br<sub>y</sub>)<sub>3</sub>

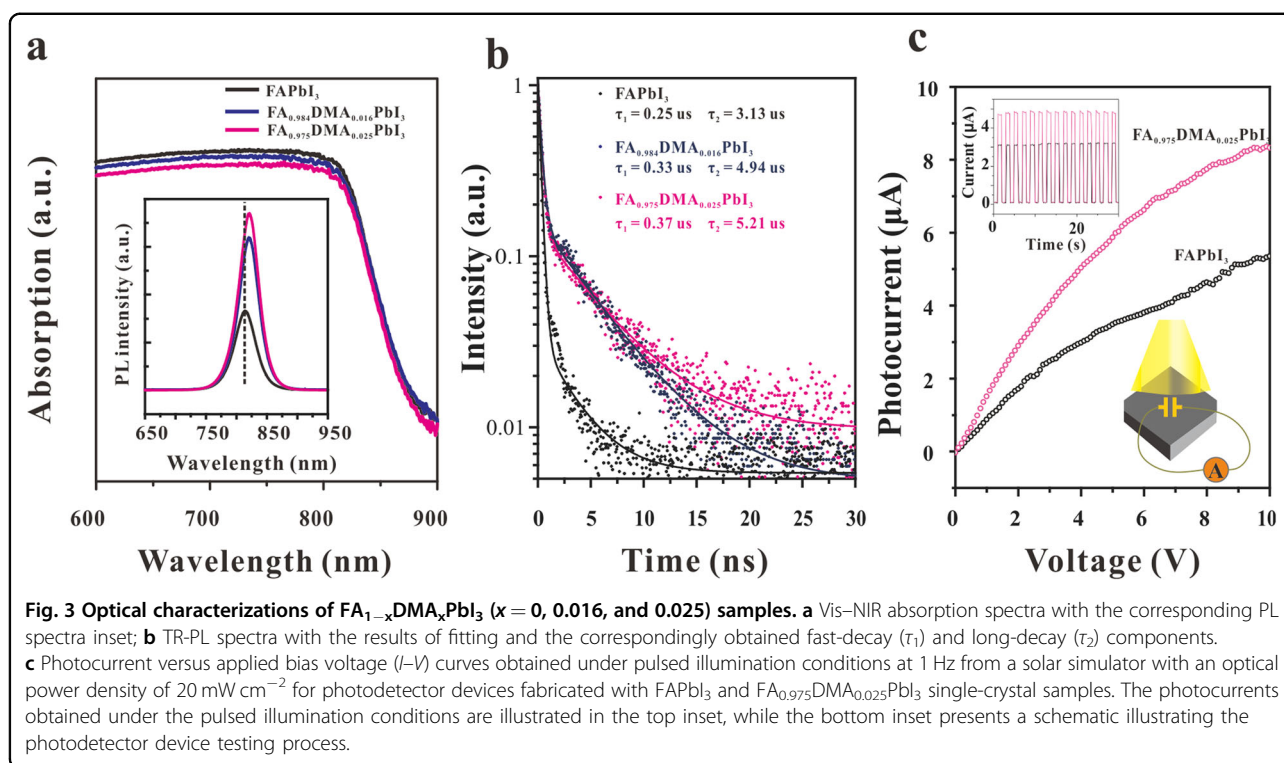
The DTA results obtained in a N<sub>2</sub> atmosphere for the FA<sub>0.975</sub>DMA<sub>0.025</sub>PbPbI<sub>3</sub>, FAPb(I<sub>0.9</sub>Br<sub>0.1</sub>)<sub>3</sub>, and FAPbI<sub>3</sub> single-crystal perovskite materials are presented in Fig. 2a. We note that the decomposition temperature of FAPb(I<sub>0.9</sub>Br<sub>0.1</sub>)<sub>3</sub> (310 °C) is far less than that of FAPbI<sub>3</sub> (328 °C), while the decomposition temperature obtained for FA<sub>0.975</sub>DMA<sub>0.025</sub>PbI<sub>3</sub> (336 °C) is much greater than that of the pure sample. These results clearly indicate that the proposed DMA substitution process can improve the thermal stability of the FAPbI<sub>3</sub> perovskite. Similar results were obtained for the FA<sub>0.984</sub>DMA<sub>0.016</sub>PbPbI<sub>3</sub> and FAPb(I<sub>0.95</sub>Br<sub>0.5</sub>)<sub>3</sub> single-crystal perovskite materials (Fig. S4).

The powder XRD results obtained for the FAPbI<sub>3</sub>, FA<sub>0.975</sub>DMA<sub>0.025</sub>PbPbI<sub>3</sub>, and FAPb(I<sub>0.9</sub>Br<sub>0.1</sub>)<sub>3</sub> perovskite materials at specific intervals of time are presented in

Fig. 2b. The middle points of 3, 24, and 18 days represent the first day when the  $\delta$ -phase of FAPbI<sub>3</sub> was detected in the corresponding XRD patterns, while the terminal points of 9, 141, and 114 days represent the first day when the  $\alpha$ -phase of FAPbI<sub>3</sub> could no longer be detected in the XRD patterns. We note that both substitution strategies greatly increase the  $\alpha$ -phase stability of FAPbI<sub>3</sub>. However, the proposed DMA substitution strategy increases the period of FAPbI<sub>3</sub>  $\alpha$ -phase stability by 24% (relative to the terminal points) to 33% (relative to the middle points) compared to that obtained by the Br substitution strategy.

#### Photovoltaic properties of FA<sub>1-x</sub>DMA<sub>x</sub>PbPbI<sub>3</sub>

The absorption spectra obtained for the FA<sub>1-x</sub>DMA<sub>x</sub>PbI<sub>3</sub> ( $x = 0, 0.016$ , and  $0.025$ ) single-crystal samples are presented in Fig. 3a. These results clearly demonstrate that the light-harvesting capability of the FAPbI<sub>3</sub> perovskite remains relatively unaffected by DMA substitution. The corresponding Tauc plots (Fig. S5) indicate that the bandgap energies of the FA<sub>1-x</sub>DMA<sub>x</sub>PbI<sub>3</sub> single-crystal samples are uniformly 1.46 eV. Interestingly, the PL spectra of the samples given in the inset of Fig. 3a present a slight redshift with increasing DMA content, which is indicative of a slight decrease in the bandgap energy. This change probably arises from the local lattice expansion caused by the larger ionic radius of DMA<sup>44,45</sup>. However, the local lattice expansions are not sufficient for altering the bandgap energy of the entire sample, such that the absorption spectra exhibit no evident change. In addition, the peak PL intensity is observed to increase substantially with increasing DMA substitution, suggesting that DMA incorporation reduces the nonradiative losses of the material due to charge carrier recombination. These results can be compared to the corresponding Vis-NIR absorption spectra and PL spectra obtained for the FAPb(I<sub>1-y</sub>Br<sub>y</sub>)<sub>3</sub> ( $y = 0, 0.05$ , and  $0.1$ ) single-crystal samples (Fig. S6a, b). According to the Tauc plots



given in the inset, the bandgap energies obtained for  $y = 0, 0.05$ , and  $0.1$  are  $1.46, 1.49$ , and  $1.52 \text{ eV}$ , respectively. Moreover, the PL spectra present an equivalent trend, and Br incorporation appears to have no effect on the non-radiative recombination losses of the materials. Accordingly, the Br substitution process does not allow the bandgap energy of the original  $\text{FAPbI}_3$  perovskite to be retained, and the optical absorption range is significantly decreased.

The effect of DMA incorporation on the charge carrier recombination process can be experimentally evaluated according to the TR-PL spectra presented in Fig. 3b. A biexponential-function fitting process was applied to the spectra to obtain two time components, including the fast-decay component ( $\tau_1$ ) and long-decay component ( $\tau_2$ ), which are included within the legend of Fig. 3b. We note that both  $\tau_1$  and  $\tau_2$  increase substantially with increasing DMA incorporation, which further demonstrates that increasing DMA incorporation progressively decreases the rates of charge carrier recombination in the  $\text{FA}_{1-x}\text{DMA}_x\text{PbI}_3$  perovskites.

The photoelectric responses of equivalently configured planar-type photodetector devices (Fig. S2) based on the  $\text{FA}_{1-x}\text{DMA}_x\text{PbI}_3$  ( $x = 0, 0.025$ ) single-crystal perovskite samples are presented in Fig. 3c as a function of applied bias voltage. The experimental testing setup is illustrated in the bottom inset of Fig. 3c, and the top inset in the figure demonstrates that the photocurrents were collected under repeated ON/OFF illumination cycles

derived from a solar simulator with an optical power density of  $20 \text{ mW/cm}^2$ . We note that the photocurrents of both photodetectors represent nonlinear responses with increasing voltage. However, the photocurrent derived from the  $\text{FA}_{0.975}\text{DMA}_{0.025}\text{PbI}_3$  single crystal increases much more rapidly with increasing bias voltage and is greater than that of the  $\text{FAPbI}_3$ -based photodetector over the entire voltage range considered. For example, the photocurrent obtained by the  $\text{FA}_{0.975}\text{DMA}_{0.025}\text{PbI}_3$  device was approximately  $5 \mu\text{A}$  at a  $4 \text{ V}$  bias, while the corresponding photocurrent of the  $\text{FAPbI}_3$  device was only  $2.5 \mu\text{A}$ .

#### Structural dynamics of $\text{FA}_{1-x}\text{DMA}_x\text{PbI}_3$ and $\text{FAPb(I}_{1-y}\text{Br}_y)_3$

The  $^2\text{H}$  NMR spectra obtained for the selectively N-deuterated  $\text{FAPbI}_3$ ,  $\text{FA}_{0.975}\text{DMA}_{0.025}\text{PbI}_3$ , and  $\text{FAPb(I}_{0.9}\text{Br}_{0.1})_3$  samples (i.e.,  $\text{FA(d4)PbI}_3$ ,  $\text{FA(d4)}_{0.975}\text{DMA}_{0.025}\text{PbI}_3$ , and  $\text{FA(N-d4)Pb(I}_{0.9}\text{Br}_{0.1})_3$ , respectively) at room temperature are presented in Fig. 4a. The three spectra differ markedly, where a single sharp peak is observed for the spectrum of  $\text{FAPbI}_3$ , which has a complicated Pake lineshape with a doublet peak separation of  $17 \text{ kHz}$ , a single sharp peak sitting in the middle of the doublet is observed for the spectrum of  $\text{FA}_{0.975}\text{DMA}_{0.025}\text{PbI}_3$ , and a single wide peak with a Gaussian lineshape is observed for the spectrum of  $\text{FAPb(I}_{0.9}\text{Br}_{0.1})_3$ .

The lineshapes of static  $^2\text{H}$  NMR spectra are known to depend strongly on molecular motions. In general, well-defined restricted molecular motions result in

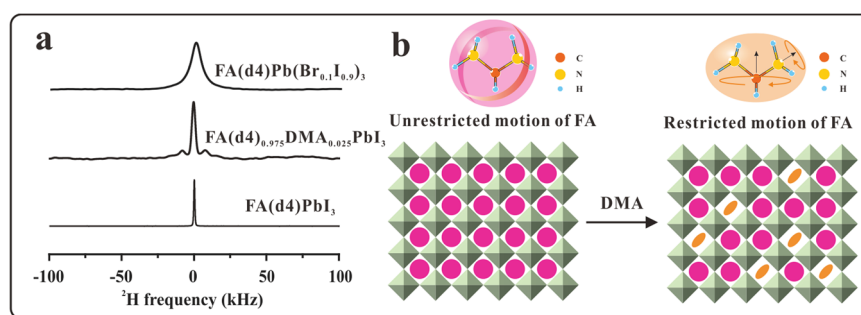


**Fig. 4** Cation dynamic characterizations of  $\text{FAPbI}_3$ ,  $\text{FA}_{0.975}\text{DMA}_{0.025}\text{PbI}_3$ , and  $\text{FAPbI}_{0.9}\text{Br}_{0.1}$  samples. **a** Static  $^2\text{H}$  NMR spectra obtained for selectively deuterated  $\text{FA}(\text{d4})\text{PbI}_3$ ,  $\text{FA}(\text{d4})_{0.975}\text{DMA}_{0.025}\text{PbI}_3$ , and  $\text{FA}(\text{d4})\text{Pb}(\text{I}_{0.9}\text{Br}_{0.1})_3$  samples at room temperature. **b** Illustration of unrestricted FA reorientation dynamics (left) and the semirestricted motion characteristic of the condition obtained after DMA substitution (right).

characteristically wide lineshapes, whereas fast unrestricted molecular motions often result in the narrowing of signal envelopes<sup>46</sup>. Therefore, the single narrow peak in the  $^2\text{H}$  NMR spectrum of  $\text{FAPbI}_3$  indicates that the FA cations likely undergo fast and unrestricted reorientation, as illustrated on the left side of Fig. 4b, which is in good agreement with the findings of previous studies<sup>47</sup>. The complicated lineshape observed for  $\text{FA}_{0.975}\text{DMA}_{0.025}\text{PbI}_3$  indicates that the reorientation dynamics of the cations are inhomogeneous and likely undergo a mixture of restricted and unrestricted motions as illustrated on the right side of Fig. 4b, where the signal component having the wide doublet lineshape is representative of some FA cations undergoing relatively slow and restricted reorientation, whereas the single narrow peak represents some FA cations undergoing fast isotropic motion. In addition, following the literature, an analysis of the spin-lattice relaxation times in Fig. S7 yields 1.23 and 1.91 ps for the correlation times of FA in  $\text{FAPbI}_3$  and  $\text{FA}_{0.975}\text{DMA}_{0.025}\text{PbI}_3$ , respectively<sup>48</sup>. This indicates that the FA cations in  $\text{FA}_{0.975}\text{DMA}_{0.025}\text{PbI}_3$  might have slower mobility than those in  $\text{FAPbI}_3$ . It should be noted that the correlation times of FA in both  $\text{FAPbI}_3$  and  $\text{FA}_{0.975}\text{DMA}_{0.025}\text{PbI}_3$  are in the picosecond range, which is far above the fast limit of the sensitive time scale of the  $^2\text{H}$  NMR lineshape analysis.

In contrast to these spectra, the single wide Gaussian peak lineshape observed for  $\text{FAPb}(\text{I}_{0.9}\text{Br}_{0.1})_3$  indicates that the cations in this case likely undergo some restricted isotropic reorientation. The observed cation motion is therefore similar to that of  $\text{FAPbI}_3$  but with a greatly reduced reorientation rate, which is possibly due to spatial restrictions arising from the distortion of the perovskite lattice after Br incorporation. In the literature, lattice distortion in Br/I lead halide perovskites has attracted considerable interest in recent years. By DFT calculations, Dou et al. revealed that the introduction of  $\text{I}^-$  anions into lead bromine perovskite may deform the crystal symmetry

and induce the clear lattice distortion of perovskite<sup>49</sup>. By ab initio molecular dynamics (MD) simulations, Boukhalov et al. reported that partial substitution of I with Br can create additional, stable lattice distortions<sup>50</sup>. The observations in these works are well in line with our observations.

The FA and DMA cation dynamics in  $\text{FA}_{0.975}\text{DMA}_{0.025}\text{PbI}_3$  were further investigated by applying temperature-dependent  $^2\text{H}$  NMR spectroscopy with selectively N-deuterated  $\text{FA}(\text{d4})\text{PbI}_3$ ,  $\text{FA}(\text{d4})_{0.975}\text{DMA}_{0.025}\text{PbI}_3$ , and C-deuterated  $\text{FA}_{0.975}\text{DMA}(\text{d6})_{0.025}\text{PbI}_3$  samples. The corresponding  $^2\text{H}$  NMR spectra acquired at different temperatures are presented in Fig. 5a–c, respectively. The phase transition of  $\text{FAPbI}_3$  from the tetragonal phase to the cubic phase occurs at 285 K<sup>51</sup>. Here, the temperatures of 245 and 280 K are associated with the tetragonal phase of  $\text{FAPbI}_3$ , whereas the temperature of 300 K is associated with the cubic phase. A comparison of Fig. 5a and b indicates that DMA substitution has very little effect on the dynamics of the FA cations at temperatures of 245 and 280 K. Both the  $\text{FAPbI}_3$  and  $\text{FA}_{0.975}\text{DMA}_{0.025}\text{PbI}_3$  samples exhibit a 40 kHz difference between the doublet peak frequencies at 245 K, which indicates that the reorientation dynamics of the FA cations are restricted completely owing to contraction in the perovskite lattice at the low temperature. The much smaller peak widths observed at a temperature of 280 K indicate that the restriction on the reorientation dynamics of the FA cations is significantly reduced at that temperature. The substantial decrease in the peak widths observed at 300 K is attributable to the phase transition of  $\text{FAPbI}_3$  from the tetragonal phase to the cubic phase at 285 K<sup>52</sup>. Accordingly, we can conclude that DMA incorporation does not alter the phase transition temperature of the perovskite lattice. However, as observed already, the reorientation dynamics of the FA cations are somewhat restricted by DMA incorporation at 280 K and 300 K compared to those observed for  $\text{FAPbI}_3$ .

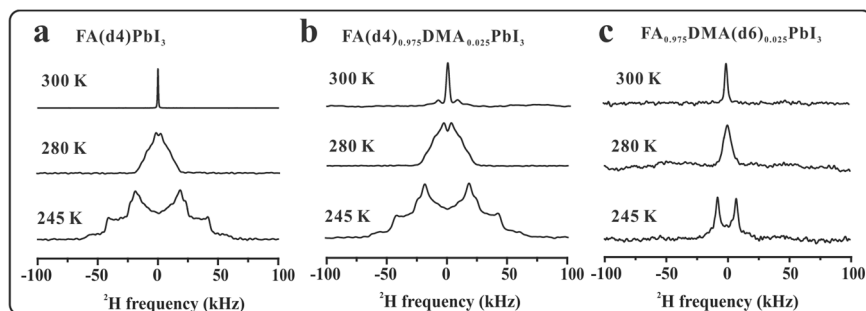


**Fig. 5** Double cation dynamics in  $\text{FA}_{0.975}\text{DMA}_{0.025}\text{PbI}_3$ . Temperature-dependent static  $^2\text{H}$  NMR spectra obtained for selectively deuterated **a**  $\text{FA}(\text{d4})\text{PbI}_3$ , **b**  $\text{FA}(\text{d4})_{0.975}\text{DMA}_{0.025}\text{PbI}_3$ , and **c**  $\text{FA}_{0.975}\text{DMA}(\text{d6})_{0.025}\text{PbI}_3$  samples.

The  $^2\text{H}$  NMR spectra in Fig. 5c obtained for the selectively C-deuterated  $\text{FA}_{0.975}\text{DMA}(\text{d6})_{0.025}\text{PbI}_3$  sample exhibit DMA reorientation dynamics that differ markedly from those associated with the FA cations in the  $\text{FA}(\text{d4})_{0.975}\text{DMA}_{0.025}\text{PbI}_3$  and  $\text{FA}(\text{d4})\text{PbI}_3$  samples. While a Pake lineshape is observed at a temperature of 245 K, the difference between the doublet peak frequencies is only 15 kHz, indicating that the reorientation dynamics of the DMA cations are less restricted at this temperature than those of the FA cations. However, a single peak with a relatively broad Gaussian lineshape is observed when the temperature increases to 280 K. As was observed in Fig. 4a for the FA cations in  $\text{FAPb}(\text{I}_{0.9}\text{Br}_{0.1})_3$ , this indicates that the DMA cations likely undergo some restricted isotropic reorientation at a reduced reorientation rate relative to that observed for  $\text{FAPbI}_3$  at room temperature. Finally, a narrow Gaussian peak is observed at 300 K, which strongly indicates that the DMA cations undergo fast isotropic reorientation.

A quite intriguing observation among these results is that the  $^2\text{H}$  NMR peaks of  $\text{FA}_{0.975}\text{DMA}(\text{d6})_{0.025}\text{PbI}_3$  are always much narrower than those of  $\text{FA}(\text{d4})_{0.975}\text{DMA}_{0.025}\text{PbI}_3$  at a given temperature, although the DMA cations have a slightly larger ionic radius than the FA cations and would therefore be expected to demonstrate more restricted dynamics. To compare the motion of the two cations more definitively, we obtained the most likely motion model of the two cations in the low-temperature phase by a simulated deuterium spectrum (Figs. S8 and 9). According to the simulated results, DMA has more motion freedom than the FA molecules in  $\text{FA}_{0.975}\text{DMA}_{0.025}\text{PbI}_3$ . This indicates that the FA cations have stronger interactions with the inorganic perovskite lattice than the DMA cations.

Another intriguing observation from the  $^2\text{H}$  NMR spectroscopy results presented herein is that DMA substitution can result in inhomogeneous cation reorientation dynamics in the samples. However, this has a twofold meaning in that the reorientation dynamics of the FA cations themselves are inhomogeneous at room

temperature and above (Fig. 5b), and they differ from those of the DMA cations at all temperatures considered (Fig. 5c). It is worth noting that the inhomogeneous cation dynamics essentially reflect an atom-level local strain in the lattice caused by the incorporation of large cations. Compared with the Br/I alloying strategies that directly change the inorganic lattice, the incorporation of large-sized cations can induce subtler strains and consequently localized distortions in the lattice. This is also supported by recent experimental and theoretical reports. For example, Ghosh et al. demonstrated that the incorporation of large cations such as DMA and GA in a  $\text{FAPbI}_3$  lattice will bring about a locally distorted low-symmetry structure by ab initio simulations<sup>53</sup>. Eperon et al. reported that the incorporation of DMA in  $\text{FA}_x\text{Cs}_{1-x}\text{PbI}_y\text{Br}_{3-y}$  perovskites will result in an octahedral tilt angle change of  $\sim 1^\circ$ <sup>54</sup>. Furthermore, Ghosh et al. found that the local lattice strain caused by cation alloying results in the restricted rotational motion of FA cations and strong FA-iodide (N—H...I) hydrogen bonding interactions<sup>55</sup>.

These observations can be readily applied for determining the mechanism by which DMA substitution affects the phase stability and photovoltaic properties of  $\text{FAPbI}_3$ . First, the relatively large size and free isotropic motion of the incorporated DMA cations compress the dynamic space of neighboring FA cations. As a result, a proportion of the FA cations will be more geometrically constrained by the surrounding inorganic lattice. The effect of this constraint is twofold. Not only does this constraint restrict FA cation motion, but it also increases the degree of interaction of FA cations with the inorganic lattice and therefore stabilizes the  $\text{PbI}_6$  lattice structure. Second, the restricted FA cation motion can be expected to reduce the strength of electron–phonon coupling by restraining the structural fluctuations of the lattice<sup>56–58</sup>. A reduced electron–phonon coupling strength is favorable for supporting a higher charge carrier mobility and a lower nonradiative electron–hole recombination rate and therefore facilitates the charge carrier collection process. Finally, the small concentration of DMA applied in the



substitution process does not lead to significant lattice distortion and therefore precludes undesirable increases in the bandgap energy and charge carrier recombination rate. This mechanism can be contrasted with that of Br substitution in FAPbI<sub>3</sub>. Here, the mismatch between the different Pb environments produced under Br substitution leads to a distortion of the PbI<sub>6</sub> lattice structure, which restricts the reorientation dynamics of the FA cations and thereby stabilizes the overall phase of the lattice structure. However, lattice disorder not only results in lower crystallinity, but significant lattice distortion also generates an unwanted change in the bandgap energy.

## Conclusion

The present work addressed the unintended consequences arising from current efforts to inhibit the spontaneous  $\alpha$ -to- $\delta$  phase transitions of organic–inorganic FAPbI<sub>3</sub> perovskites based on simple cation and anion substitution strategies by applying an ultratrace DMA substitution strategy for FAPbI<sub>3</sub>-based PSC applications. The results of rigorous analyses demonstrated that the proposed DMA substitution strategy can significantly improve the phase stability and photoelectric response of FAPbI<sub>3</sub> perovskite materials, while the inherent bandgap energy of the FAPbI<sub>3</sub> perovskite is maintained. The results of <sup>2</sup>H NMR spectroscopy clearly demonstrated that the relatively large size and free isotropic motion of incorporated DMA cations constrain the dynamic space of neighboring FA cations, which not only restricts FA cation motion but also increases the degree to which FA cations interact with the inorganic lattice and therefore stabilizes the PbI<sub>6</sub> lattice structure without significant lattice distortion. Moreover, the restricted FA cation motion reduces the strength of electron–phonon coupling, which supports a higher charge carrier mobility and a lower non-radiative electron–hole recombination rate and therefore facilitates the charge carrier collection process. Finally, in contrast to the Br substitution strategy, the small concentration of DMA applied in the substitution process does not lead to significant lattice distortion and therefore precludes undesirable increases in the bandgap energy and charge carrier recombination rate.

## Acknowledgements

This work was supported by the National Natural Science Foundation of China (Grant Nos. 22072045, 21603073, and 21574043), Xing-Fu-Zhi-Hua Foundation of ECNU, and Microscale Magnetic Resonance Platform of ECNU.

## Author contributions

Y.-F.Y. conceived the project and designed the experiments. W.-C.Q. and J.-Q.L. produced the samples. W.-C.Q. and J.-Q.L. carried out the structural stability experiments. W.-C.Q. and W.D. developed the optoelectronic devices and conducted the device tests. X.L.W., K.M., W.-C.Q., and Y.-F.Y. analyzed the XRD, NMR, PL, and Vis-NIR experimental data. W.-C.Q., X.L.W., and Y.-F.Y. wrote the manuscript. All authors discussed the results and commented on the manuscript.

## Data availability

All data required to evaluate the conclusions in the paper are presented in the paper and/or the Supplementary Materials. Additional data related to this paper may be requested from the authors.

## Conflict of interest

The authors declare no competing interests.

## Publisher's note

Springer Nature remains neutral with regard to jurisdictional claims in published maps and institutional affiliations.

**Supplementary information** The online version contains supplementary material available at <https://doi.org/10.1038/s41427-022-00395-3>.

Received: 28 October 2021 Revised: 7 April 2022 Accepted: 11 April 2022  
Published online: 10 June 2022

## References

- Lee, M. M., Teuscher, J., Miyasaka, T., Murakami, T. N. & Snaith, H. J. Efficient hybrid solar cells based on meso-superstructured organometal halide perovskites. *Science* **338**, 643–647 (2012).
- Snaith, H. J. Perovskites: The emergence of a new era for low-cost, high-efficiency solar cells. *J. Phys. Chem. Lett.* **4**, 3623–3630 (2013).
- Kojima, A., Teshima, K., Shirai, Y. & Miyasaka, T. Organometal halide perovskites as visible-light sensitizers for photovoltaic cells. *J. Am. Chem. Soc.* **131**, 6050–6051, <https://doi.org/10.1021/ja809598r> (2009).
- Yuan, M. et al. Perovskite energy funnels for efficient light-emitting diodes. *Nat. Nanotechnol.* **11**, 872–877 (2016).
- Lin, K. et al. Perovskite light-emitting diodes with external quantum efficiency exceeding 20 percent. *Nature* **562**, 245–248 (2018).
- Wang, H. et al. A multi-functional molecular modifier enabling efficient large-area perovskite light-emitting diodes. *Joule* **4**, 1977–1987 (2020).
- Dou, L. et al. Solution-processed hybrid perovskite photodetectors with high detectivity. *Nat. Commun.* **5**, 1–6 (2014).
- Dong, R. et al. High-gain and low-driving-voltage photodetectors based on organolead triiodide perovskites. *Adv. Mater.* **27**, 1912–1918 (2015).
- Saidaminov, M. I. et al. Planar-integrated single-crystalline perovskite photodetectors. *Nat. Commun.* **6**, 1–7 (2015).
- Dong, Q. et al. Electron-hole diffusion lengths > 175  $\mu$ m in solution-grown CH<sub>3</sub>NH<sub>3</sub>PbI<sub>3</sub> single crystals. *Science* **347**, 967–970 (2015).
- Zhumekeov, A. A. et al. Formamidinium lead halide perovskite crystals with unprecedented long carrier dynamics and diffusion length. *ACS Energy Lett.* **1**, 32–37 (2016).
- You, P., Li, G., Tang, G., Cao, J. & Yan, F. Ultrafast laser-annealing of perovskite films for efficient perovskite solar cells. *Energy Environ. Sci.* **13**, 1187–1196 (2020).
- Yoo, J. J. et al. Efficient perovskite solar cells via improved carrier management. *Nature* **590**, 587–593 (2021).
- NREL. Best Research-Cell Efficiency Chart <https://www.nrel.gov/pv/cell-efficiency.html> (2022).
- Liu, Y. et al. Stabilization of highly efficient and stable phase-pure FAPbI<sub>3</sub> perovskite solar cells by molecularly tailored 2D-overlayers. *Angew. Chem. Int. Ed.* **59**, 15688–15694 (2020).
- Min, H. et al. Efficient, stable solar cells by using inherent bandgap of  $\alpha$ -phase formamidinium lead iodide. *Science* **366**, 749–753 (2019).
- Akin, S., Akman, E. & Sonmezoglu, S. FAPbI<sub>3</sub>-based perovskite solar cells employing hexyl-based ionic liquid with an efficiency over 20% and excellent long-term stability. *Adv. Funct. Mater.* **30**, 2002964 (2020).
- Huang, Y., Lei, X., He, T., Jiang, Y. & Yuan, M. Recent progress on formamidinium-dominated perovskite photovoltaics. *Adv. Energy Mater.* **12**, 2100690 (2021).
- Han, Q. et al. Single crystal formamidinium lead iodide (FAPbI<sub>3</sub>): Insight into the structural, optical, and electrical properties. *Adv. Mater.* **28**, 2253–2258 (2016).
- Lu, H. et al. Vapor-assisted deposition of highly efficient, stable black-phase FAPbI<sub>3</sub> perovskite solar cells. *Science* **370**, eabb8985 (2020).

21. McMeekin, D. P. et al. A mixed-cation lead mixed-halide perovskite absorber for tandem solar cells. *Science* **351**, 151–155 (2016).
22. Saliba, M. et al. Cesium-containing triple cation perovskite solar cells: improved stability, reproducibility, and high efficiency. *Energy Environ. Sci.* **9**, 1989–1997 (2016).
23. Jeon, N. J. et al. A fluorene-terminated hole-transporting material for highly efficient and stable perovskite solar cells. *Nat. Energy* **3**, 682–689 (2018).
24. Li, Z. et al. Stabilizing perovskite structures by tuning tolerance factor: formation of formamidinium and cesium lead iodide solid-state alloys. *Chem. Mater.* **28**, 284–292 (2016).
25. Park, Y. H. et al. Inorganic rubidium cation as an enhancer for photovoltaic performance and moisture stability of HC (NH<sub>2</sub>)<sub>2</sub>PbI<sub>3</sub> perovskite solar cells. *Adv. Funct. Mater.* **27**, 1605988 (2017).
26. Jiang, Q. et al. Surface passivation of perovskite film for efficient solar cells. *Nat. Photonics* **13**, 460–466 (2019).
27. Binek, A., Hanusch, F. C., Docampo, P. & Bein, T. Stabilization of the trigonal high-temperature phase of formamidinium lead iodide. *J. Phys. Chem. Lett.* **6**, 1249–1253 (2015).
28. Rehman, W. et al. Charge-carrier dynamics and mobilities in formamidinium lead mixed-halide perovskites. *Adv. Mater.* **27**, 7938–7944 (2015).
29. Heo, J. H., Choi, Y. K., Koh, C. W., Woo, H. Y. & Im, S. H. Semitransparent FAPbI<sub>3</sub>-xBr<sub>x</sub> perovskite solar cells stable under simultaneous damp heat (85 °C/85%) and 1 sun light soaking. *Adv. Mater. Technol.* **4**, 1800390 (2019).
30. Chen, L. et al. Toward long-term stability: single-crystal alloys of cesium-containing mixed cation and mixed halide perovskite. *J. Am. Chem. Soc.* **141**, 1665–1671 (2019).
31. Yao, D. et al. Hindered formation of photoinactive  $\delta$ -FAPbI<sub>3</sub> phase and hysteresis-free mixed-cation planar heterojunction perovskite solar cells with enhanced efficiency via potassium incorporation. *J. Phys. Chem. Lett.* **9**, 2113–2120 (2018).
32. Lyu, M. & Park, N.-G. Effect of additives AX (A = FA, MA, Cs, Rb, NH<sub>4</sub>, X = Cl, Br, I) in FAPbI<sub>3</sub> on photovoltaic parameters of perovskite solar cells. *Sol. RRL* **4**, 2000331 (2020).
33. Ye, H.-Y. et al. Metal-free three-dimensional perovskite ferroelectrics. *Science* **361**, 151–155 (2018).
34. Hoke, E. T. et al. Reversible photo-induced trap formation in mixed-halide hybrid perovskites for photovoltaics. *Chem. Sci.* **6**, 613–617 (2015).
35. Zhou, C. et al. Illumination-induced halide segregation in gradient bandgap mixed-halide perovskite nanoplatelets. *Adv. Optical Mater.* **6**, 1801107 (2018).
36. Gao, X. X. et al. Stable and high-efficiency methylammonium-free perovskite solar cells. *Adv. Mater.* **32**, 1905502 (2020).
37. Ke, W., Spanopoulos, I., Stoumpos, C. C. & Kanatzidis, M. G. Myths and reality of HPbI<sub>3</sub> in halide perovskite solar cells. *Nat. Commun.* **9**, 1–9 (2018).
38. Goldschmidt, V. M. Die Gesetze der Kristallochemie. *Naturwissenschaften* **14**, 477–485 (1926).
39. Maheshwari, S., Patwardhan, S., Schatz, G. C., Renaud, N. & Grozema, F. C. The effect of the magnitude and direction of the dipoles of organic cations on the electronic structure of hybrid halide perovskites. *PCCP* **21**, 16564–16572 (2019).
40. Kieslich, G., Sun, S. & Cheetham, A. K. Solid-state principles applied to organic–inorganic perovskites: New tricks for an old dog. *Chem. Sci.* **5**, 4712–4715 (2014).
41. Zhao, J. et al. Mechanism of the dimethylammonium cation in hybrid perovskites for enhanced performance and stability of printable perovskite solar cells. *Solar RRL* <https://doi.org/10.1002/solr.202100923>.
42. Askar, A. M. et al. Composition-tunable formamidinium lead mixed halide perovskites via solvent-free mechanochemical synthesis: Decoding the Pb environments using solid-state NMR spectroscopy. *J. Phys. Chem. Lett.* **9**, 2671–2677 (2018).
43. Rosales, B. A. et al. Persistent dopants and phase segregation in organolead mixed-halide perovskites. *Chem. Mater.* **28**, 6848–6859 (2016).
44. Filip, M. R., Eperon, G. E., Snaith, H. J. & Giustino, F. Steric engineering of metal-halide perovskites with tunable optical band gaps. *Nat. Commun.* **5**, 1–9 (2014).
45. Amat, A. et al. Cation-induced band-gap tuning in organohalide perovskites: Interplay of spin–orbit coupling and octahedra tilting. *Nano Lett.* **14**, 3608–3616 (2014).
46. Bernard, G. M. et al. Methylammonium cation dynamics in methylammonium lead halide perovskites: A solid-state NMR perspective. *J. Phys. Chem. A* **122**, 1560–1573 (2018).
47. Kubicki, D. J. et al. Cation dynamics in mixed-cation (MA)<sub>x</sub>(FA)<sub>1–x</sub>PbI<sub>3</sub> hybrid perovskites from solid-state NMR. *J. Am. Chem. Soc.* **139**, 10055–10061 (2017).
48. Franssen, W. M., van Heumen, C. M. & Kentgens, A. P. Structural investigations of MA<sub>1–x</sub>DMA<sub>x</sub>PbI<sub>3</sub> mixed-cation perovskites. *Inorg. Chem.* **59**, 3730–3739 (2020).
49. Dou, Y. et al. Lattice distortion in mixed-anion lead halide perovskite nanorods leads to their high fluorescence anisotropy. *ACS Mater. Lett.* **2**, 814–820 (2020).
50. Boukhvalov, D. W. et al. Thermal effects and halide mixing of hybrid perovskites: MD and XPS studies. *J. Phys. Chem. A* **124**, 135–140 (2019).
51. Weber, O. J. et al. Phase behavior and polymorphism of formamidinium lead iodide. *Chem. Mater.* **30**, 3768–3778 (2018).
52. Fabiani, D. H. et al. Reentrant structural and optical properties and large positive thermal expansion in perovskite formamidinium lead iodide. *Angew. Chem.* **128**, 15618–15622 (2016).
53. Ghosh, D. et al. Lattice expansion in hybrid perovskites: Effect on optoelectronic properties and charge carrier dynamics. *J. Phys. Chem. Lett.* **10**, 5000–5007 (2019).
54. Eperon, G. E. et al. The role of dimethylammonium in bandgap modulation for stable halide perovskites. *ACS Energy Lett.* **5**, 1856–1864 (2020).
55. Ghosh, D., Smith, A. R., Walker, A. B. & Islam, M. S. Mixed A-cation perovskites for solar cells: Atomic-scale insights into structural distortion, hydrogen bonding, and electronic properties. *Chem. Mater.* **30**, 5194–5204 (2018).
56. Gong, X. et al. Electron–phonon interaction in efficient perovskite blue emitters. *Nat. Mater.* **17**, 550–556 (2018).
57. Huang, Y. et al. A-site cation engineering for highly efficient MAPbI<sub>3</sub> single-crystal X-ray detector. *Angew. Chem. Int. Ed.* **58**, 17834–17842 (2019).
58. Fu, Y. et al. Incorporating large A cations into lead iodide perovskite cages: Relaxed goldschmidt tolerance factor and impact on exciton–phonon interaction. *ACS Cent. Sci.* **5**, 1377–1386 (2019).